

Supplementary Information for

Longitudinally thickness-controlled nanofilms on exposed core fibres enabling spectrally flattened supercontinuum generation

Authors

Tilman A. K. Lühder ¹, Henrik Schneidewind ¹, Erik P. Schartner ², Heike Ebendorff-Heidepriem ², and Markus A. Schmidt* ^{1,3,4}

¹ Leibniz Institute of Photonic Technology, Albert-Einstein-Str. 9, 07745 Jena, Germany

² School of Physical Sciences and ARC Centre of Excellence for Nanoscale BioPhotonics (CNBP) and Institute for Photonics and Advanced Sensing (IPAS), The University of Adelaide, Adelaide SA 5005, Australia

³ Otto Schott Institute of Material Research, Fraunhoferstr. 6, 07743 Jena, Germany

⁴ Abbe School of Photonics and Physics Faculty, Friedrich Schiller University, 07743 Jena, Germany

*markus-alexander.schmidt@uni-jena.de

Layer fabrication

Ta was sputtered with 200 W dc at 0.5 Pa in an Ar atmosphere with 30 % O₂ content. No heating or annealing ensures all layers to be amorphous in order to lower the surface roughness to ~0.2 nm RMS (atomic force microscope measurements on a 2 μm area without bigger particles, Fig. S1c) and minimise scattering losses¹. The RMS roughness including bigger particles is about 2 nm. Variations of the layer refractive index could be caused by different Ar concentrations in the film², changing stoichiometry³ or morphology and void formation at high substrate angles.

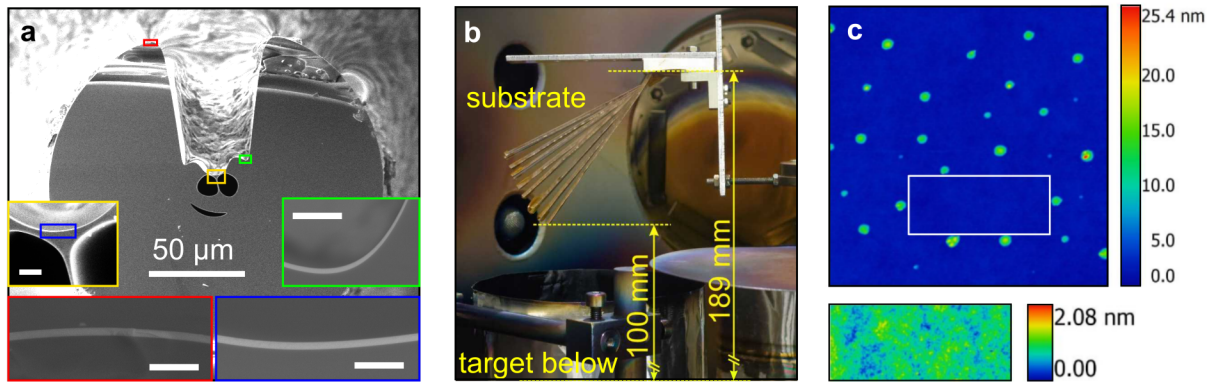


Figure S1: (a) SEM of the ECF cross section with insets of the magnified core (yellow, scale bar 2 μm) and three positions showing details of the Ta₂O₅ layer (scale bars 500 nm). (b) Photograph of the bronze substrate holder inside the sputtering deposition chamber with individual fingers at 27.5° to 51.8° (steepest finger unused). (c) 5x5 μm AFM micrograph of the roughness measurement of the 35° B33 substrate with a magnified particle free section.

A SEM of the full fibre cross section can be seen in Fig. S1a. The groove of the fibre giving access to the core needs to be aligned with the sputtering direction in order to successfully deposit nanofilms on the core. A possible nanofilm inside the two enclosed air holes is irrelevant since both fibre ends, where some deposition could occur, are cleaved before the optical measurements. SEM images of the layer at different positions of the fibre are shown in insets. As there are collisions of the Ta atoms with the sputtering gas this deposition technique is not purely

directed. Combined with non-vertical side walls and an extended Ta target of 10 cm diameter, this causes a thin layer to be deposited on the side walls of the groove. Its thickness is at the thinnest position $\sim 20\%$ of the maximum possible thickness, measured on the outside of the fibre (red inset). This ratio f_c of nanofilm thickness inside the fibre groove compared to on a planar substrate increases towards the center of the groove, reaching up to 85-90% at the core region (two test samples). Although having an acceptance angle of 40° , corresponding to accepting non-scattered atoms originating from all over the Ta target at a distance of 11 cm or more, f_c varies as the fibre is not aligned perfectly at experimentally realised target distances ranging from 11 to 18.5 cm (substrate is longer than the fibre in Fig. S1b). Furthermore, it may depend on the substrate angle and distance to the target, varying longitudinally along the length of one fibre. For simulations, f_c was assumed to be constant throughout a single fibre but was kept as a variable to match simulations and experiments. On top of it, the curved core surface leads to a lateral change in layer thickness, which was accounted for by modeling a constant layer thickness in vertical direction instead of perpendicular to the core surface.

Pulse propagation simulation

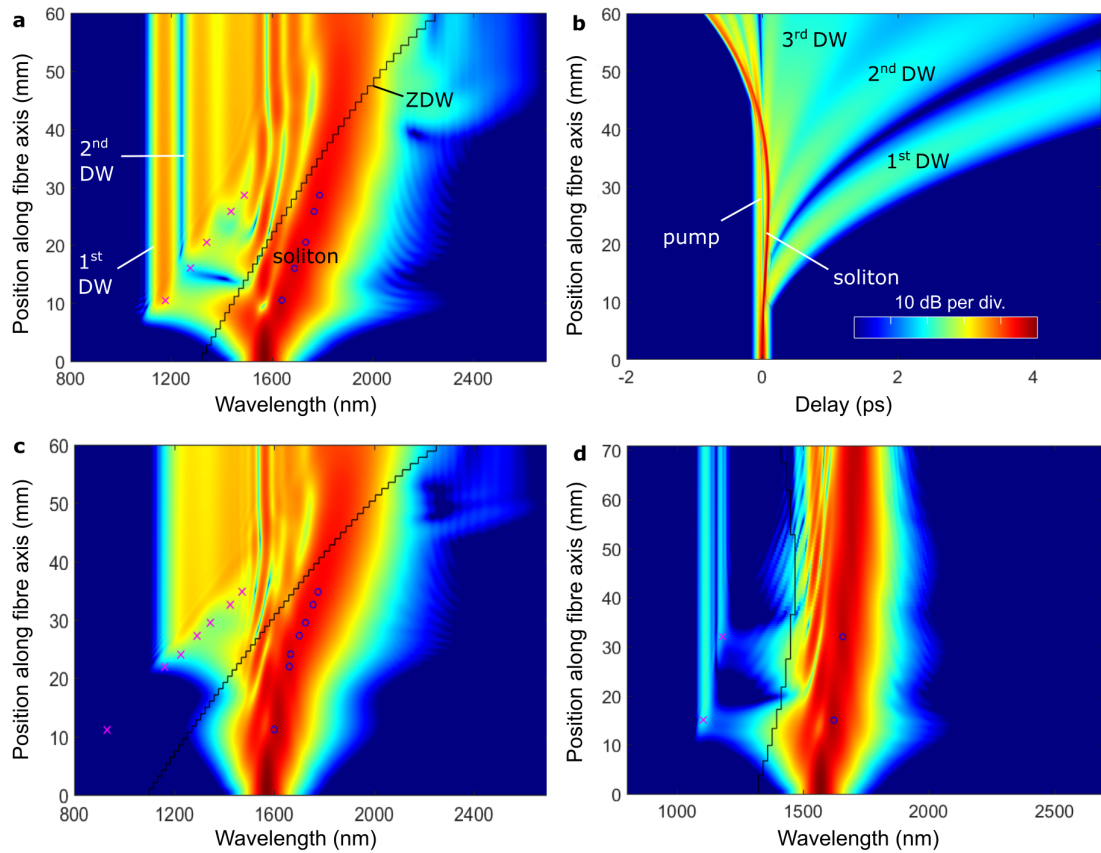


Figure S2: Nonlinear pulse propagation simulations. Spectral (a) and temporal (b, normalised to the pump wavelength) pulse evolution along a fibre with linear nanofilm thickness gradient from 63 to 105 nm at 9.5 kW peak power and 3 dB cm^{-1} losses. (c) Same as in (a) but with 50 nm starting thickness. (d) Pulse propagation of the 8° fibre (brown line of Fig. 4c, 7 kW peak power, 2 dB cm^{-1} losses). The black line shows the ZDW at each position along the fibre and magenta crosses mark the phase-matching wavelength using the soliton wavelength (blue circles).

Pulse propagation simulations solving the GNLSE of a fibre with a linear gradient from 63 to 105 nm nanofilm thickness are shown in Fig. S2a-b. In the temporal domain a single soliton and the formation of multiple DWs are clearly visible. The first DW is created at around 8 mm fibre length. Within the first three cm of the fibre the soliton red-shifts along the ZDW before crossing it. Only near this crossing the soliton number forms a singularity and rises above 2. Here, higher order soliton fission into multiple fundamental solitons would be possible. At the fibre position 45 mm from the fibre start the soliton splitting into multiple branches can be seen in simulations in Fig. S2b. However, this temporal splitting does not affect the spectrum within the bandwidth definition and could also be caused by the temporal overlap of the soliton with the remaining pump pulse. Spectral features at the long wavelength side in simulations (Fig. S2a+c) are not observable in experiments and are not considered when calculating the FoM of simulations.

When reducing the starting thickness to 50 nm (Fig. S2c), the primary DW is skipped (usually created at a fibre length of ~ 10 mm) as explained in the main article, reducing the bandwidth but enhancing spectral flatness. The first observable DW is created 25 mm from the fibre start.

Having only a minor gradient from 62 to 70 nm nanofilm thickness as in the brown curve of Fig. 4c (8° fibre), the soliton Raman shift is reduced (Fig. S2d).

Using the appropriate phase-matching equation⁴, the possible wavelengths of the dispersive waves along the fibre can be predicted. Through the visible match between experimental DW peaks and corresponding simulations, this verifies that all DWs observed result from the same soliton (Fig. S2). For these calculations, the soliton peak power is assumed to match the input peak power regardless of the fibre position (λ_s : soliton wavelength (blue circles)).

FoM breakdown

In Fig. S3 the individual contributions of $\log(\text{RMS})$ and bandwidth to the FoM of Fig. 3c is separated, revealing the origin of the FoM maxima A and B. The -30 dB DW detection edge is clearly visible in both parts.

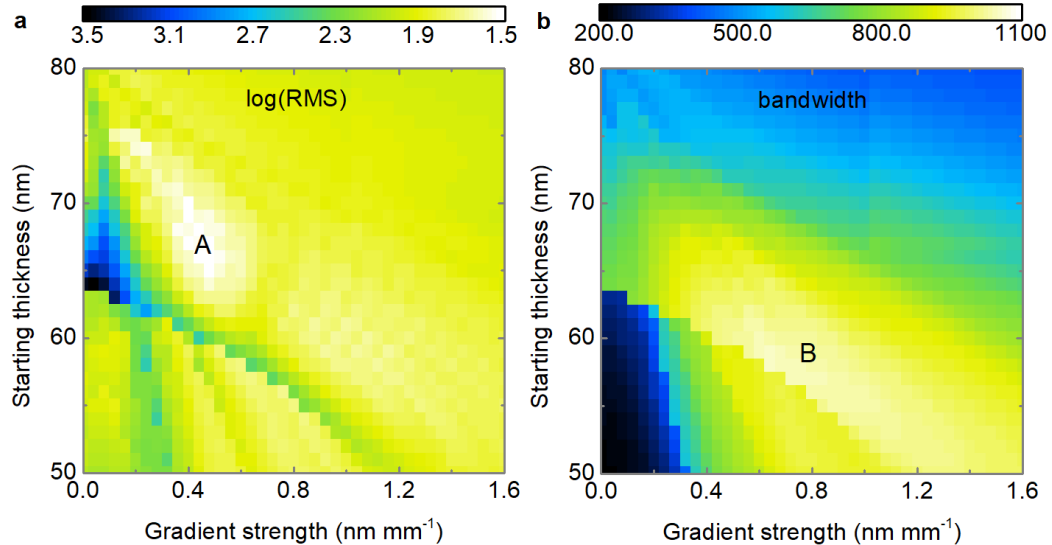


Figure S3: Starting thickness and gradient strength influence on $\log(\text{RMS})$ (a) and bandwidth [nm] (b) for linear thickness gradients on a 7.5 cm long fibre. Best values are marked with A and B.

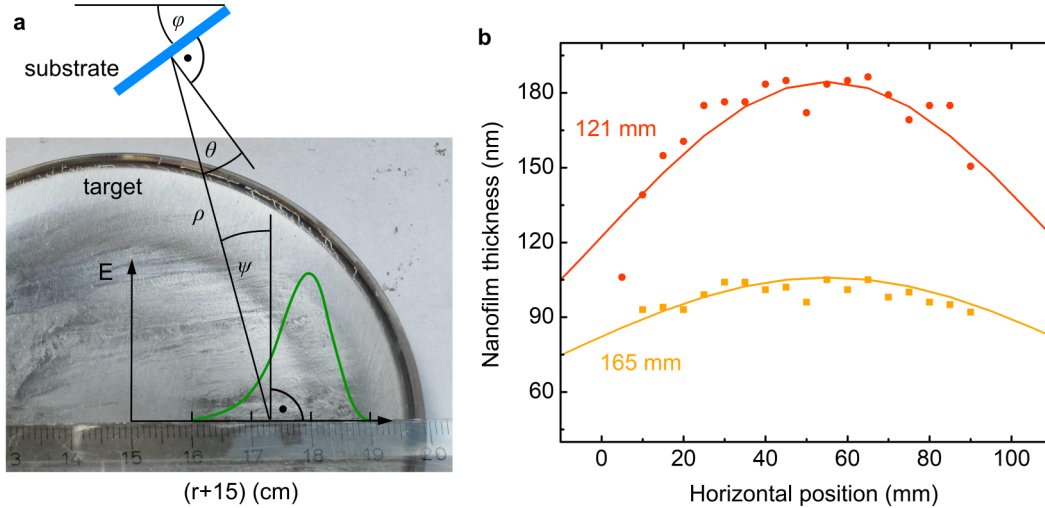


Figure S4: (a) Two dimensional schematic of the sputtering model described in the text with a photograph of the Ta target erosion. (b) Experimental (dots) and fitted model thicknesses (lines) on two horizontal Si wafers at substrate-target-distances of 121 and 165 mm.

Sputtering model

Our sputtering model is based on Fan et al.⁵ and adapted for angled substrates⁶ as used by Yu et al.⁷ The total thickness of each point on the substrate $T(\vec{x})$ has some contribution from every part of the Target weighted with the target erosion function $E(\vec{r})$ and considering the angular evaporation dependence $A(\psi) = \sin(\psi)^p$ of the target. Furthermore, it decreases quadratically with distance ρ and has a cos like dependence on the impact angle θ on the substrate.

$$T(\vec{x}) = A_0 \int_{Target} \frac{E(\vec{r})A(\psi) \cos(\theta)}{\rho^2} dA \quad (1)$$

The erosion function was estimated from the target visually to be radial symmetric poisson distribution shaped with Γ symbolising the Gamma function: $E(r) = \left[1.5 \frac{8 \text{ cm} - 2r}{\Gamma(8 \text{ cm} - 2r)} + 0.0045 (r - 4 \text{ cm}) \right]^{1.5}$. Parameters are indicated in a 2D sketch in Fig. S4a. Secondary effects such as scattering on the sputtering gas in between the Target and the substrate, resputtering, reflection, biased and kinetic energy assisted diffusion⁸ are neglected. The parameters $p = 2.51$ and $A_0 = 0.014 \text{ s}^{-1}$ where obtained by fitting the model to measured thicknesses of Ta_2O_5 layers (P-10 surface profiler, KLA-Tencor Corp.) along two parallel to the target placed Si wafers at 121 and 165 mm distance (Fig. S4b). Please note that the lateral alignment of the substrate relative to the target center was also kept as a variable for parameter fitting and fitting of simulated thicknesses to experimental data.

fibres losses

fibres losses were experimentally measured by the cutback method. A broadband light source (SuperK Compact, NKT Photonics Inc.) was coupled into the ECF with a 20x objective. Without changing the incoupling condition, the fibre was cut at the outcoupling side and the transmitted light before and after cutting was collected by a butt-coupled P1-980A (Thorlabs Inc.) fibre and measured with a spectrometer (AQ6374, Yokogawa Corp.). High losses near 700 nm for the 73 nm and near 900 nm for the 115 nm thick coated fibre (Fig. S5a) are connected to

the anti-crossing wavelength (compare to Fig 2a). We account absorption of adsorbed water and OH groups in the silica core for the ~ 1400 nm peak.

Figure S5b shows the simulated influence of spectrally constant losses along the fibre independent of layer thickness on the final spectra on the example of the 26.5° fibre (10.8 kW peak power, 28 fs pump pulse at 1570 nm, nanofilm gradient of orange solid line in Fig. 4c). Although the first DW remains nearly unaffected, the soliton blue shifts with increasing losses and correspondingly impacts the connected secondary DWs. Higher losses reduce the bandwidth and the FoM of the spectrum. Since the major contribution of constant losses solely affect the soliton, this study also gives insight to the effects in the case more realistic wavelength dependent losses would be considered, i.e. losses being higher for longer wavelengths. The higher losses for the soliton impose a smaller Raman shift and a decrease of its power as can be seen by the difference of simulated and experimental data of Figs. 5c-d and Figs. 5f-g.

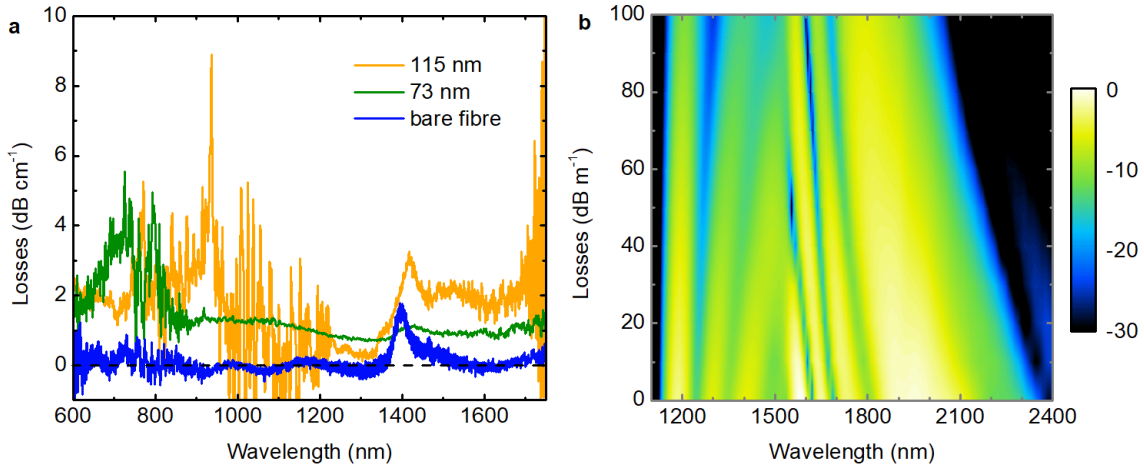


Figure S5: (a) Experimentally measured fibre losses for ECFs with constant nanofilm thickness compared to the fibre without nanofilm. (b) Simulated influence of constant losses on the spectrum (color scale in dB) for the 26.5° fibre (10.8 kW peak power, 28 fs pump pulse at 1570 nm, nanofilm gradient of orange solid line in Fig. 4c).

Additional mode properties and applications

Increasing thickness of the nanofilm on the fibre core changes the modal properties, leading to an modified effective mode area, an increasing fraction of electric field interacting with the nanofilm and a larger fraction of evanescent field outside the nanofilm area. To demonstrate the impact of the nanofilm, the mode field area and the fraction of power inside the various spatial domains of the mode for a fixed wavelength of 1.6 μm are displayed in Fig. S6. The effective area increases for $t < 90$ nm due to the extension of the evanescent field until the counteracting effect of modal confinement inside the nanofilm becomes dominant for thick nanofilms. Including the nanofilm to the ECF the evanescent power located in the air region close to the nanofilm compared to the total evanescent power in all three air regions rises from one third to 88 % at 110 nm thickness (a factor of 5 in absolute value). This makes our fibre attractive for applications in sensing and photochemistry. Note that the electric field inside the nanofilm increases with thicker layers and makes coating materials with a two level electronic configuration interesting for soliton self-induced transparency studies. Moreover, the ECF concept has been used for tuneable third harmonic generation⁹ and as a waveguide platform for 2D materials¹⁰.

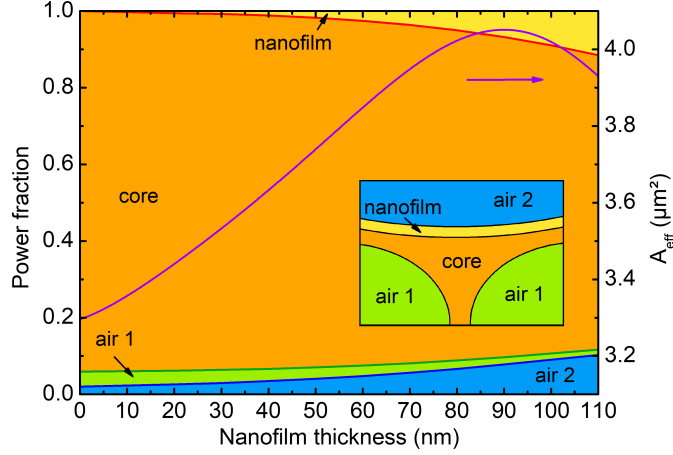


Figure S6: Simulated effective mode field area A_{eff} and fraction of the power within different spatial domains of the mode dependent on the nanofilm thickness at $\lambda = 1.6 \mu\text{m}$. The different domains are defined in the schematic inset, showing a cross-section of the fibre core region.

Spectral stability and coherence

Pulse-to-pulse stability is simulated by adding phase and amplitude variations to the input spectrum. The noise includes a 10^{11} -fold multiplied one photon per mode with random phase model¹¹ (creating a noise floor of -44 dB) combined with random peak power and pulse duration variations up to 2 %, which is realistic for mode-locked fibre lasers at the telecommunications wavelength¹². A total of 20 simulations, each of which include a different input spectrum, were calculated. All 190 combinations of independent simulations (fields E_i and E_j , $i, j \in [1, 20]$, $i \neq j$) contribute to the ensemble averaged first-order degree of coherence calculation¹³.

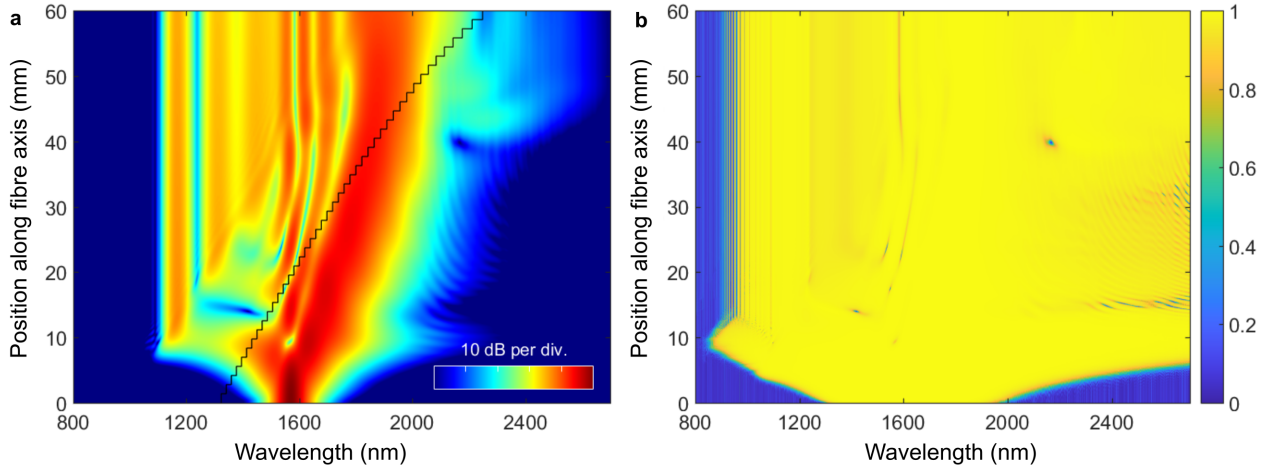


Figure S7: (a) Averaged spectral evolution of 20 simulations with a linear gradient from $t = 63$ to $t = 105 \text{ nm}$ ($gs = 0.7 \text{ nm mm}^{-1}$) with noise explained in the text. The ZDW is marked by a black line. (b) Ensemble first-order coherence of (a).

$$|g_{i,j}^{(1)}| = \langle |E_i|^* \cdot |E_j| \rangle \cdot (\langle |E_i|^2 \rangle \langle |E_j|^2 \rangle)^{-0.5} \quad (2)$$

To demonstrate the coherence properties of our approach, the averaged spectrum of a fibre that includes a linear gradient from 63 to 105 nm ($gs = 0.7 \text{ nm mm}^{-1}$) nanofilm thickness at 9.5 kW input power (same as in Fig. S2a) and the corresponding evolution of the coherence are shown in Fig. S7. The coherence is close to unity almost across the entire spectral evolution, confirming excellent pulse-to-pulse stability and coherence, which is not possible to achieve with modulation instability related broadening approaches.

References

1. Wu, S. J., Houg, B. & Huang, B. Effect of growth and annealing temperatures on crystallization of tantalum pentoxide thin film prepared by rf magnetron sputtering method. *Journal of Alloys and Compounds* **475**, 488 – 493 (2009).
2. Chang, P.-H. & Liu, H.-Y. Structures of tantalum pentoxide thin films formed by reactive sputtering of Ta metal. *Thin Solid Films* **258**, 56 – 63 (1995).
3. Demiryont, H., Sites, J. R. & Geib, K. Effects of oxygen content on the optical properties of tantalum oxide films deposited by ion-beam sputtering. *Applied Optics* **24**, 490–495 (1985).
4. Agrawal, G. P. *Nonlinear Fiber Optics*. 4th edn. (San Diego: Academic Press, 1995).
5. Fan, Q., Chen, X. & Zhang, Y. Computer simulation of film thickness distribution in symmetrical magnetron sputtering. *Vacuum* **46**, 229 – 232 (1995).
6. Broadway, D. M., Platonov, Y. Y. & Gomez, L. A. Achieving desired thickness gradients on flat and curved substrates. Proceedings of SPIE 3766, X-Ray Optics, Instruments, and Missions II. Denver, CO, United States: SPIE, 1999.
7. Yu, B. et al. Control of lateral thickness gradients of Mo-Si multilayer on curved substrates using genetic algorithm. *Optics Letters* **40**, 3958–3961 (2015).
8. Sun, S. et al. Mo/Si multilayers sputtered onto inclined substrates: experiments and simulations. *Optics Express* **28**, 13516–13531 (2020).
9. Warren-Smith, S. C. et al. Tunable multi-wavelength third-harmonic generation using exposed-core microstructured optical fiber. *Optics Letters* **44**, 626–629 (2019).
10. Ngo, G. Q. et al. Scalable functionalization of optical fibers using atomically thin semiconductors. *Advanced Materials* **32**, 2003826 (2020).
11. Frosz, M. H. Validation of input-noise model for simulations of supercontinuum generation and rogue waves. *Optics Express* **18**, 14778–14787 (2010).
12. Huang, P. L. et al. Stable mode-locked fiber laser based on CVD fabricated graphene saturable absorber. *Optics Express* **20**, 2460–2465 (2012).
13. Dudley, J. M., Genty, G. & Coen, S. Supercontinuum generation in photonic crystal fiber. *Reviews of Modern Physics* **78**, 1135–1184 (2006).